

# PHOTONICS Research

## Interdigitated terahertz metamaterial sensors: design with the dielectric perturbation theory

LEI CAO,<sup>1,2</sup>  FANQI MENG,<sup>2,\*</sup>  ESRA ÖZDEMİR,<sup>2</sup> YANNIK LOTH,<sup>3</sup> MERLE RICHTER,<sup>3</sup> ANNA KATHARINA WIGGER,<sup>3</sup> MAIRA BEATRIZ PÉREZ SOSA,<sup>4</sup> ALAA JABBAR JUMA AH,<sup>4</sup>  SHIHAB AL-DAFFAIE,<sup>4</sup> PETER HARING BOLÍVAR,<sup>3</sup>  AND HARTMUT G. ROSKOS<sup>2,5</sup> 

<sup>1</sup>State Key Laboratory of Advanced Electromagnetic Technology, Huazhong University of Science and Technology, Wuhan 430074, China

<sup>2</sup>Physikalisches Institut, Johann Wolfgang Goethe-Universität, Frankfurt am Main, Germany

<sup>3</sup>University of Siegen, Institute for High Frequency and Quantum Electronics, Siegen, Germany

<sup>4</sup>Department of Electrical Engineering, Eindhoven University of Technology, 5612 AE Eindhoven, The Netherlands

<sup>5</sup>e-mail: roskos@physik.uni-frankfurt.de

\*Corresponding author: fmeng@physik.uni-frankfurt.de

Received 15 December 2023; revised 14 February 2024; accepted 4 March 2024; posted 4 March 2024 (Doc. ID 516228); published 17 May 2024

Designing terahertz sensors for highly sensitive detection of nanoscale thin films and a few biomolecules poses a substantial challenge but is crucial for unlocking their full potential in scientific research and advanced applications. This work presents a strategy for optimizing metamaterial sensors in detecting small quantities of dielectric materials. The amount of frequency shift depends on intrinsic properties (electric field distribution,  $Q$ -factor, and mode volume) of the bare cavity as well as the overlap volume of its high-electric-field zone(s) and the analyte. Guided by the simplified dielectric perturbation theory, interdigitated electric split-ring resonators (ID-eSRRs) are devised to significantly enhance the detection sensitivity compared with eSRRs without interdigitated fingers. ID-eSRR's fingers redistribute the electric field, creating strongly localized enhancements, which boost analyte interaction. The periodic change of the inherent antiphase electric field reduces radiation loss, leading to a higher  $Q$ -factor. Experiments with ID-eSRR sensors operating at around 300 GHz demonstrate a remarkable 33.5 GHz frequency shift upon depositing a 150 nm SiO<sub>2</sub> layer as an analyte simulant, with a figure of merit improvement of over 50 times compared with structures without interdigitated fingers. This rational design offers a promising avenue for highly sensitive detection of thin films and trace biomolecules. © 2024 Chinese Laser Press

<https://doi.org/10.1364/PRJ.516228>

### 1. INTRODUCTION

Optical sensors are indispensable in diverse applications, ranging from detecting nanoscale thin films and nanoparticles [1–3] to identifying biomolecules, viruses, and cells [4–6]. Elevating sensor efficacy, particularly by intensifying the interaction between light and matter and enhancing sensitivity, holds the potential to unlock groundbreaking applications. Therefore, advancing the capabilities of optical sensors is crucial. Metamaterials (MMs) are artificial periodic structures with subwavelength features. Their response to electromagnetic radiation can be controlled by their structural design and the materials they are composed of [7]. The strong local electric field enhancement by the subwavelength mode concentration makes MMs ideal candidates for sensing analytes. The exploration of applications of MMs for sensing has been flourishing in the last two decades. We concentrate here on planar metallic MMs used at terahertz (THz) frequencies [8–13]. Frequently used unit-cell structures of metallic MMs consist of square or

circular split-ring resonators (SRRs) [14,15], asymmetric double-split-ring resonators (aDSRRs) [8–10], electric split-ring resonators (eSRRs) [12,16], I-shaped structures [17], and coupled structures with two or more resonators [18–24]. Although THz sensors based on metallic MMs have shown advantages in terms of contact- and label-free detection [25,26], they still have disadvantages in terms of sensitivity and detection limits compared with existing mature and standardized biochemical diagnostic methods such as enzymatic immunoassays [27,28]. Therefore, further improvements in the sensitivity of THz sensors are a crucial task in order to make this sensing method competitive for practical applications.

It is widely accepted that optimized MM sensors should exhibit a strong local electric field enhancement at the location of the analyte, a high-quality factor ( $Q$ -factor) to ensure a narrow spectral resonance for reliable identification of a resonance shift, and a small mode volume, an aspect recently recognized as a key parameter, in order to achieve a large overlap of the

electric field with the analyte [17]. However, a systematic and practical optimization strategy that coherently considers all the parameters for the rational design of MM sensors has been missing until now.

Another shortcoming in this field of sensor research relates to the performance indicators usually employed. For the assessment of the relative performance of MM sensors, two parameters find application. The first is the refractive index sensitivity, often denoted by the letter  $S$ , which is calculated as the resonance frequency shift resulting from a change in the refractive index of the analyte by unity (and hence is measured in units of “GHz/RIU,” RIU standing for “refractive index unit”). The second indicator is the figure of merit (FOM), calculated as the ratio of  $S$  to the full width at half maximum (FWHM) of the resonance line in the power spectrum (and hence is measured in units of RIU<sup>-1</sup>) [29]. The problem with these parameters is that they only allow the comparison of sensitivities among various sensors if the analyte is applied at the same location and in the same amount, which means thin films should be applied with the same layer thickness. However, this is often disregarded in the literature, as will be shown later.

This work, for the first time to our best knowledge, systematically addresses these two issues. Regarding the first, we apply the dielectric perturbation theory to quantitatively guide the rational design of planar MM sensors. Our proposed solution, the interdigitated electric split-ring resonator (ID-eSRR) with minigaps, integrates interdigitated fingers with split-ring MM resonators, proving to be an optimized structure for thin-film detection. The ID-eSRR not only significantly enhances the detection sensitivity but also boosts the  $Q$ -factor compared with the eSRR without fingers. Experimental validation demonstrates a remarkable improvement of the FOM by more than a factor of 50, which lets our ID-eSRR outperform existing MM-based THz sensors for thin-film detection in terms of sensitivity and FOM. With regard to the second issue, it also becomes apparent that it is often unconvincing to compare sensors using only those two conventional performance parameters ( $S$  and FOM). One should design different sensors for different types of analytes and employ different performance parameters. For analytes brought onto the sensor in the form of continuous thin films, we suggest a third performance indicator obtained by normalizing the FOM by the thickness of the film. We term this indicator a TN-FOM (abbreviation for “thickness-normalized FOM”).

## 2. STRATEGY FOR THE RATIONAL DESIGN OF MM SENSORS

The property used for sensing is the frequency shift of one or several resonant modes due to the dielectric load of the analyte. To increase sensitivity, it is necessary to locally enhance the electric field and compact the mode volume at the respective resonance frequencies [17]. Dielectric perturbation theory is widely employed in the microwave community to predict the resonance frequency shift of cavities [30,31]. We extend this theory to the THz frequency range and propose a strategy to predict the resonance frequency shift of MM sensors.

In general, the relative change in resonance frequency caused by a nonmagnetic analyte in an MM resonator can be calculated analytically:

$$\frac{\Delta f}{f_0} = -\frac{\Delta W}{W_0} = \frac{-\int_{\Delta V} \Delta \epsilon |\vec{E}_0|^2 dV}{\int_V \epsilon |\vec{E}_0|^2 dV + \int_V \mu |\vec{H}_0|^2 dV}. \quad (1)$$

Here,  $W_0$  represents the energy (electric energy  $W_e$  and magnetic energy  $W_m$ ) stored in the cavity without the analyte, and  $\Delta W$  is the change in that energy due to the presence of the analyte.  $\vec{E}_0$  and  $\vec{H}_0$  denote the electric and magnetic field distributions, and  $\mu$  and  $\epsilon$  represent the permeability and permittivity of the filling medium (or media) in the resonator (effective cavity volume  $V$ ), all before the introduction of the analyte.  $\Delta \epsilon$  indicates the relative change in permittivity associated with the analyte, which occupies the volume  $\Delta V$ , compared with the original filling medium. All quantities in Eq. (1), including  $\vec{E}_0$ ,  $\vec{H}_0$ ,  $\mu$ ,  $\epsilon$ , and  $\Delta \epsilon$ , are implicitly understood to be spatially dependent functions [ $F = F(\vec{r})$ ]. The equation is derived under the assumption that the electric field distribution of the respective resonator mode is only weakly perturbed by the analyte, and the tangential component of the electric field is null at the boundary of the resonator (the boundary in the case of MMs is the delimiter of the unit cell; in our simulations, we extend the vertical boundaries out to 30  $\mu\text{m}$  above (air) and below (substrate) the surface of the substrate [17,31]). According to Eq. (1), the frequency shift caused by the analyte depends on the size of the volume  $\Delta V$  occupied by the analyte and the spatial dependence of the electric field in the cavity volume (volume integration, giving relevance to the electric field enhancement factor).

The stored electric energy and magnetic energy are almost equal at the resonance frequency, as confirmed in the simulations. The denominator on the right side of Eq. (1) can hence be approximated as  $\int_V \epsilon |\vec{E}_0|^2 dV + \int_V \mu |\vec{H}_0|^2 dV = 2 \int_V \epsilon |\vec{E}_0|^2 dV$ . At the resonance frequency of the MM structure, the electric field is mainly concentrated in and at the splits (gaps) of the metallic resonators and especially at the corners of the metal edges. By reducing the width of the gaps, the local electric field is enhanced, and the mode volume is reduced, both of which usually lead to improvement in sensitivity [32–34].

If we assume the analyte to be sufficiently thin and positioned in the region of the maximum electric field, and if the electric field there is assumed to be uniform, Eq. (1) can be simplified to

$$\frac{\Delta f}{f_0} \approx \frac{-\Delta \epsilon \max[|\vec{E}_0|^2] \cdot d \cdot A}{2 \int_V \epsilon |\vec{E}_0|^2 dV} = \frac{-\Delta \epsilon \cdot d \cdot A}{2 \epsilon_s V_{\text{eff}}}. \quad (2)$$

Here,  $d$  is the thickness of the analyte layer, and  $A$  represents the overlap area between the analyte and the region of high electric field.  $V_{\text{eff}}$  in the denominator on the right side of Eq. (2) is the mode volume, which quantifies the spatial extent of the electric field of the resonance mode. It is defined by [35]

$$V_{\text{eff}} = \frac{\int_V \epsilon |\vec{E}_0|^2 dV}{\max[\epsilon_s |\vec{E}_0|^2]} \quad (3)$$

as the ratio of the total electric energy of the mode and the maximal value of the electric energy density [ $\epsilon |\vec{E}_0|^2$ ], whose

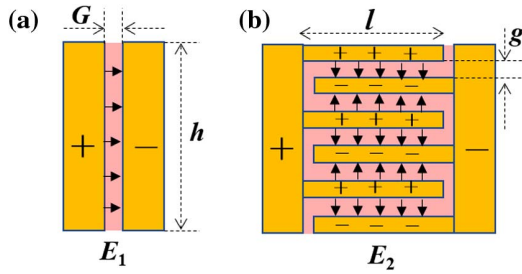


**Fig. 1.** Schematics of two gap structures used in SRRs: (a) 1D slot-like gap; (b) 2D interdigitated gap structure. The areas plotted in pink color represent the regions with high electric field. If  $G = g$  and if the same voltages are applied, the electric fields in the gap regions in (a) and (b) are of similar magnitude.

location is usually in the substrate with the dielectric constant  $\epsilon_s$ .

The value of  $A$  in Eq. (2) depends on the field distribution of the MM sensor and the way in which the analyte is deposited. For our approach, we use the fact that the electric field in many MM structures is concentrated around the metal edges bordering the gaps of the metallic resonators (compare the two cases in Fig. 1; pink, high-field regions in the gap between the metallic edges). Since the electric field distribution is inhomogeneous, a possible way to define the bounds of the high-field region is to specify a delimiter where the electric field amounts to 10% of the maximal strength of the electric field [8]. If the analyte is deposited homogeneously as a thin layer covering the whole surface of the MM (which would also be a good assumption in the case of a homogeneous film of dried viral or cellular biomaterial [12,36]), then  $A$  is the area of overlap between the region of high electric field and the analyte layer. If, on the other hand, the analyte covers only a small area within the high-field region, then  $A$  equals the area covered by the analyte.

According to Eq. (2), a small value of  $V_{\text{eff}}$  helps enhance the frequency shift. The shift is larger if more of the field is concentrated in the analyte. The straightforward way to achieve field concentration is by reducing the width of the gap in the MM structure. This has been explored in the literature [12,32–34]. In the experiments of Ref. [12], for example, an eSRR MM structure was used as a sensor for uniformly dried virus layers. When the gap width was reduced from 3  $\mu\text{m}$  to 200 nm, the sensitivity increased by a factor of 13.

Another important quantity is the linewidth of the resonance ( $Q$ -factor). The larger the  $Q$ -factor, the easier the frequency shift can be recognized. With the refractive index  $n_a$  of the analyte ( $n_a \neq 1$ ), one obtains the sensitivity as  $S = |\Delta f / \Delta n| = |\Delta f / (n_a - 1)|$ ; using Eq. (2), the FOM value can be approximately expressed as

$$\text{FOM} = \frac{S}{\text{FWHM}} \approx \frac{\Delta\epsilon \cdot d \cdot A}{2\Delta n} \cdot \frac{Q}{V_{\text{eff}} \cdot \epsilon_s}. \quad (4)$$

The first fraction in Eq. (4) is determined by the parameters of the analyte and the second by the properties of the MM resonator. The FOM is often used to compare the performance of different sensors. However, this is problematic due to the

first fraction. The thickness, overlap area, and refractive index of the analyte all change the FOM, making the comparison of different sensors difficult when they are intended for analytes with differing properties. As a universal parameter for the comparison of sensors, the FOM should be analyte-independent.

In the microwave sensor community, the sensitivity is not normalized by the refractive index unit ( $\Delta n$ ) but instead by the permittivity unit ( $\Delta\epsilon$ ) [37,38]. Then, Eq. (4) can be further simplified because  $\Delta\epsilon$  appears in the numerator and the denominator. The influence of the refractive index (resp. the permittivity) is then eliminated. If one further normalizes by the overlap volume ( $d \cdot A$ ), then a new figure of merit is obtained, which contains only the second fraction in Eq. (4),  $Q / (V_{\text{eff}} \epsilon_s)$ . Such a figure of merit does not depend on the analyte and only reflects the performance of the sensor. For the universal comparison of sensors, this quantity represents a well-suited performance parameter [17]. This is especially true and useful for the design of sensors for monitoring minute traces of an analyte (such as biochemicals down to ultra-low molecule concentrations) located only in the high-electric-field region of the sensors.

In the following, we will concentrate on MM sensors, where thin analyte films are homogeneously deposited over the whole surface of the sensor. We assume that the thickness of the film is known. For this specific case, we introduce a thickness-normalized FOM (TN-FOM), obtained by dividing the conventional FOM by the thickness of the analyte film. To remain consistent with the common practice of the THz MM sensing community, we continue normalizing  $S$  and the FOM by the refractive index unit. With Eq. (4), the TN-FOM is

$$\text{TN-FOM} = \frac{\text{FOM}}{d} = \frac{\Delta\epsilon \cdot A}{2\Delta n} \cdot \frac{Q}{V_{\text{eff}} \cdot \epsilon_s}. \quad (5)$$

This quantity is useful for sensor comparison even if analyte materials are different. As the analyte is deposited as a continuous layer, the overlap area  $A$  is determined by the field distribution on the SRR and can hence be considered a property of the sensor itself. Having discussed various performance parameters, we now analyze Eq. (4), respectively, and Eq. (5), regarding ways to improve the sensors. One way to achieve this is by the choice of a substrate with a low dielectric constant  $\epsilon_s$ . This measure has already been explored in the literature [39]. We do not pursue this option further in the present paper.

As discussed above, with a smaller gap comes a smaller high-field region  $A$  (overlap area), but the ratio  $A / V_{\text{eff}}$  in the equations significantly increases because  $V_{\text{eff}}$  is inversely proportional to the maximum electric field, which scales inversely with the width of the gap [32–34]. Now, the question arises whether an extension of the length  $l$  of the gap, for example, by giving it a meandering shape as indicated in Fig. 1, could improve the value of the TN-FOM if one keeps the gap width fixed. At first glance, this should not be the case. If we approximate the overlap area  $A$  by the gap area, then an increase in the length of the gap will linearly raise the value of  $A$  ( $A \propto l$ ). However, it is straightforward to also assume a more or less linear increase in the value of  $V_{\text{eff}}$  ( $V_{\text{eff}} \propto l$ ) because one does not expect a significant change in the electric field strength and its vertical extension for a fixed gap width.  $A / V_{\text{eff}}$  would remain approximately constant. However, the numerical evaluation of  $V_{\text{eff}}$  for real MM structures shows otherwise.

In the following section of this publication, we investigate an eSRR MM with a meandering gap structure (ID-eSRR) in simulations and experiments.

Field simulations show that the interdigitated structure exhibits a mode volume of  $26 \mu\text{m}^3$  vs. the  $10 \mu\text{m}^3$  for the eSRR MM with a slot-like gap (cp. Table 2).  $V_{\text{eff}}$  hence has increased by a factor of 2.6, while the length of the gap and its area are about 8.8 times larger. The ratio  $A/V_{\text{eff}}$  (again approximating  $A$  by the gap width) has increased by a factor of 3.4. According to Eq. (5), this promises an enhanced TN-FOM.

It is worth mentioning that the potential for sensor improvement by lengthening the gap arises from an unexpectedly strong difference between the high-field volume and the mode volume. This difference can be illustrated approximately by calculating how much of the mode volume lies outside the gap area. The results of such calculations are presented in the Appendix C, for the ID-eSRR and eSRR investigated in detail below. For the slot-like gap of the eSRR, we find that, despite the strong field enhancement, most of the mode volume (in our case, more than 98%) lies outside the gap area. Using a meandering gap brings much more of the mode volume into the gap area (in our case, 11.6%). This leads to the predicted sensor improvement.

Another parameter in Eq. (5) that can be optimized is the  $Q$ -factor. There are various ways how  $Q$  can be improved, e.g., by the use of Fano MMs [40,41] or bound state in the continuum (BIC) MMs [42–44]. We will not address such options here. We only point out that the use of interdigitated fingers in the gap leads also to a substantial increase in  $Q$ . Conventional eSRR MMs with a slot-like gap possess a relatively low  $Q$ -factor due to radiation loss [45]. The introduction of an interdigitated finger structure reduces the radiation loss. The reason is that a significant part of the emission of radiation arises from the gap region. In an interdigitated structure, the dipoles of adjacent minigaps have opposite polarity [as indicated by the black arrows in Fig. 1(b)]; thus, the far-field radiation loss is substantially suppressed. For our structures, the simulations predict that the  $Q$ -factor of the ID-eSRR MM is  $4\times$  larger than that of the eSRR MM with the slot-like gap.

### 3. RESULTS

#### A. Interdigitated eSRR (ID-eSRR) MM Sensors

Figure 2 shows the structure of the proposed THz sensor based on an interdigitated electric split-ring resonator (ID-eSRR) on a

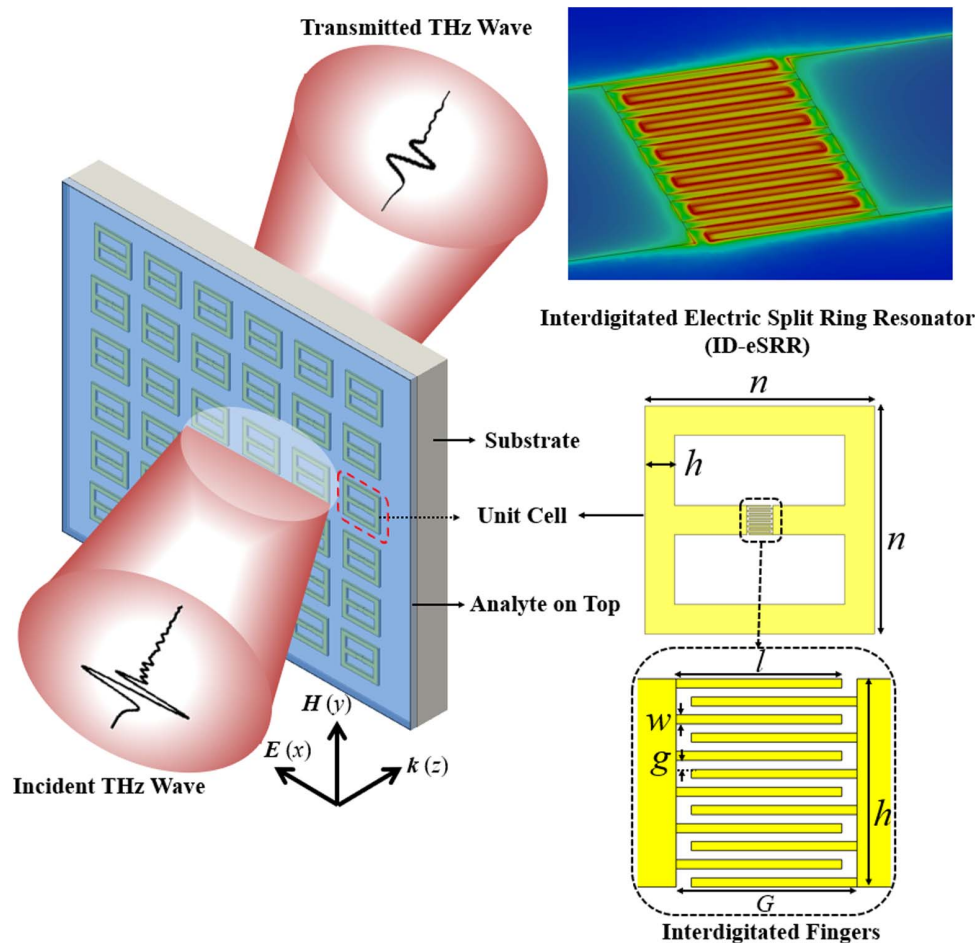


**Fig. 2.** Proposed interdigitated electric split-ring-resonator (ID-eSRR) MMs for THz sensing applications. In the unit cell structure,  $n$  is the size of the square ID-eSRR,  $h$  the width of the metal stripes,  $G$  the gap width,  $l$  the finger length,  $w$  the finger width, and  $g$  the width of the minigap between adjacent fingers.

**Table 1. Structural Parameters (in  $\mu\text{m}$ ) of the ID-eSRR and eSRR MM Sensors Working at 300 GHz**

	eSRR		
	ID-eSRR	eSRR ( $G = 0.6 \mu\text{m}$ )	eSRR ( $G = 12 \mu\text{m}$ )
Period ( $p$ )	240	240	240
Metal stripe length ( $n$ )	107	150	168
Metal stripe width ( $h$ )	13.8	13.8	13.8
Gap width ( $G$ )	12	0.6	12
Finger length ( $l$ )	11	—	—
Finger width ( $w$ )	0.6	—	—
Minigap width ( $g$ )	0.6	—	—

fused silica substrate. We investigate this structure and compare its properties with those of two traditional eSRR structures, also on fused silica, exhibiting different gap lengths.

The structural parameters of the ID-eSRR and traditional eSRR MMs are listed in Table 1. They are chosen such that the resonance frequency  $f_0$  of the fundamental  $LC$  mode of all structures is close to 300 GHz. All devices have square-shaped unit cells with a side length of  $p = 240 \mu\text{m}$  and the metal stripes forming the SRRs have a width of  $h = 13.8 \mu\text{m}$  in all cases.

Of the two traditional eSRR structures, one has a wide gap with the same extension ( $G = 12 \mu\text{m}$ ) as the large gap of the ID-eSRR MM. The other structure has a narrow gap ( $G = 0.6 \mu\text{m}$ ) with an extension corresponding to the width of the minigap ( $g$ ) of the ID-eSRR structure.

In the ID-eSRR structure with its six pairs of fingers, the finger length ( $l = 11 \mu\text{m}$ ) is  $1 \mu\text{m}$  shorter than the gap width ( $G = 12 \mu\text{m}$ ), while the finger width ( $w$ ) and the minigap width ( $g$ ) between adjacent fingers remain at a constant value of  $0.6 \mu\text{m}$ . In terms of the equivalent circuit model for the  $LC$  resonance mode, the capacitance ( $C$ ) is primarily determined by the gap region's geometry, while the inductance ( $L$ ) mainly arises from the metal stripes (with dimensions  $h, n$ ) [45,46].

For the ID-eSRR structure, the equivalent capacitance is high due to the large number of finger capacitors in parallel to each other (a total of 11 minigaps), with the value of each capacitor determined by the minigap width ( $g$ ). Consequently, the equivalent inductance must be lower than that of the traditional eSRR structures to maintain the same resonance

**Table 2. Resonance Frequency, Q-factor, Resonance Depth, and Mode Volume for the ID-eSRR and eSRR MMs**

	ID-eSRR	eSRR ( $G = 0.6 \mu\text{m}$ )	eSRR ( $G = 12 \mu\text{m}$ )
$f_0$ (GHz)	296.3	297.5	296.9
$Q$	43.1	11.0	5.8
$Q_R$	113.7	12.5	6.2
$Q_C$	71.0	89.9	99.6
$Q_D$	3380.3	3122.5	1909.6
$T_r$	0.42	0.56	0.49
$V_{\text{eff}}$ ( $\mu\text{m}^3$ )	26	10	420

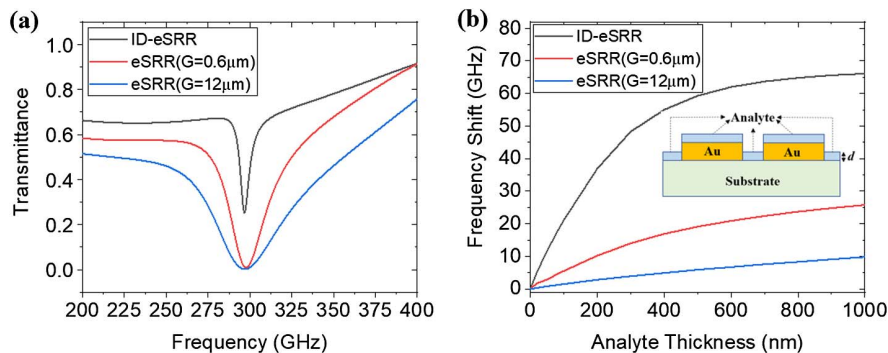
frequency. This is achieved by shortening the metal stripes (length  $n$ ).

Figure 3(a) depicts the spectra of the ID-eSRR MM (black line) and the eSRR structures on fused silica (red and blue lines). Comparing the two eSRR structures with each other, one finds that the one with the narrower gap has a sharper resonance than the one with the wider gap. However, the resonance line of the ID-eSRR structure, while not being the deepest, is found to be the sharpest of all three transmittance resonances, indicating that the  $Q$ -factor of that structure is higher than those of the two eSRR structures. This feature is beneficial for accurately identifying the resonance frequency during measurements.

Table 2 provides a summary of the properties of the resonance lines of the three structures: the resonance frequency; the  $Q$ -factor and its constituents; and the depth of the resonance. The  $Q$ -factor is composed of three contributions, which combine to the total  $Q$ -factor according to

$$\frac{1}{Q} = \frac{1}{Q_R} + \frac{1}{Q_C} + \frac{1}{Q_D}. \quad (6)$$

The three contributions reflect different sources of loss: radiation loss (determining the  $Q$ -factor component  $Q_R$ ); conduction or ohmic loss (responsible for  $Q_C$ ); and dielectric loss (leading to  $Q_D$ ). The values of the individual  $Q$ -contributions are calculated by numerically varying the material properties of the metal (gold or perfect electrical conductor "PEC") and the substrate (lossy or loss-free) in the simulations. We then verified that the resultant value of  $Q$  is equal



**Fig. 3.** (a) Transmittance spectra of the bare ID-eSRR and eSRR MMs. (b) Refractive index sensing: frequency shift as a function of analyte thickness ( $d$ ). Inset shows the location of the analyte in all simulations. The analyte material is  $\text{SiO}_2$  ( $\epsilon_r = 3.75 + j \cdot 0.0004$ ).

to the value obtained by fitting the resonance curve with a Lorentzian function.

For all the structures, the value of  $Q_D$  is one or two orders of magnitude higher than  $Q_R$  or  $Q_C$ , indicating that dielectric loss in the substrate is negligible compared with the total losses of the MM structures themselves. Among the three structures, the ID-eSRR exhibits the highest value of  $Q$  (43.1), while the eSRR structure with a large gap value ( $G = 12 \mu\text{m}$ ) has an extremely low  $Q$ -value (5.8). For both eSRR structures, radiation loss dominates the total loss, whereas, in the ID-eSRR structure, conduction loss is the dominant factor.

To quantitatively evaluate the radiation loss, a single resonator of ID-eSRR and eSRR with a perfect conductor suspended in air is excited with a current source, and the far-field radiation pattern is captured on a sphere placed 1 m away from the resonator. With the introduction of interdigitated fingers, the radiation power density ( $\text{W}/\text{m}^2$ ) can be reduced by 10 dB from the simulation results of the electric dipole radiation pattern (additional details included in Appendix A). Regarding the resonance depth  $T_r$  (absolute value of the difference between the maximum and minimum transmittance around the resonance frequency), the ID-eSRR structure has a lower value compared with the two eSRR structures.

We now compare the mode volumes of the three types of eSRR structures. To determine the mode volumes, we first calculate the field distributions. The six top panels of Figs. 4(a)–4(c) display the distribution of the electric field amplitude at the height (200 nm) of the metal surface for the three structures at the respective resonance frequency. In the large-gap eSRR structure [Fig. 4(c)], the strongest electric field is found primarily concentrated near the metal edges of the gap. As the gap width decreases from 12 to  $0.6 \mu\text{m}$ , the maximum electric field amplitude increases by a factor of five.

The eSRR structure with the narrow gap [ $G = 0.6 \mu\text{m}$ ; Fig. 4(b)] exhibits a high electric field covering an area approximately equal to the gap area ( $A = b \times G = 8.28 \mu\text{m}^2$ ).

Similarly in the ID-eSRR structure [Fig. 4(a)], the field amplitude reaches about the same peak value (the electric field distribution along the  $z$  axis is provided in Appendix B), and the electric field is also concentrated over the entire gap region, which in this case consists of the 11 meandering minigaps, covering an area of about  $A = 11 \times l \times g = 72.6 \mu\text{m}^2$ . The high-electric-field area hence has increased by 8.8 times by the introduction of the interdigitated fingers. Consequently, this leads to a larger numerator in Eq. (2), and significantly larger frequency shifts can be expected upon analyte sensing.

Before continuing with the mode volume, we point out a feature of the field distribution that is important for sensing applications. The three panels at the bottom of Fig. 4 display 2D cuts through the 3D electric fields along the red dashed lines shown in the middle row of panels. There is a remarkable feature in Figs. 4(a) and 4(b): the electric field in the gaps is mainly concentrated in the air (or the vacuum) between the metal edges and only weakly extends into the substrate. This feature is attributed to the reduction of the fringing field as the distance between the metal edges ( $0.6 \mu\text{m}$ ) decreases to a similar scale to the height of the metal edges ( $0.2 \mu\text{m}$ ). The benefit of this field concentration is that it is in the free space of the gaps and is available for interaction with an analyte.

We now turn to the mode volume of the three types of structures. Table 2 lists the values of the mode volume calculated with Eq. (3) for the three structures. The mode volume of the small-gap eSRR structure ( $10 \mu\text{m}^3$ ) is only 2.4% of that of the large-gap eSRR structure ( $420 \mu\text{m}^3$ ). By introducing interdigitated fingers, the mode volume of the ID-eSRR structure is raised to  $26 \mu\text{m}^3$ , which amounts to 2.6 times the mode volume of the small-gap eSRR structure. Expressed in terms of the resonance wavelength  $\lambda_0$  in free space, it is equal to  $2.6 \times 10^{-9} \times \lambda_0^3$ .

It is apparent that the mode volume does not increase as rapidly as the area  $A$ . The reason is that the electric energy contained within the gaps is only a small portion of the total energy

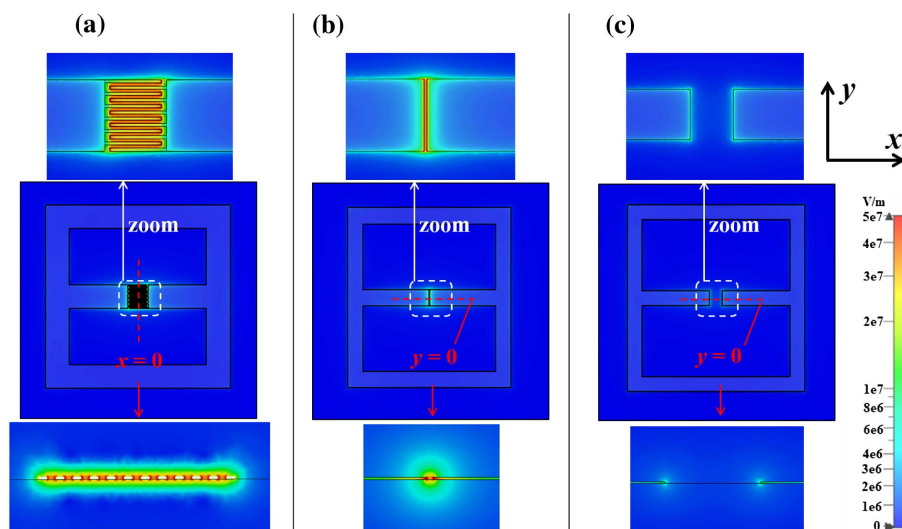


**Fig. 4.** Two top rows of panels: Electric field distribution in the plane of the metal surface at the respective resonance frequency for the three structures: (a) ID-eSRR; (b) eSRR ( $G = 0.6 \mu\text{m}$ ); and (c) eSRR ( $G = 12 \mu\text{m}$ ). Bottom row of panels: Cuts through the 3D electric field distribution along the red dashed lines shown in the middle row of panels. The amplitude of the incident electric field is  $8.09 \times 10^4 \text{ V}/\text{m}$  for all structures.

**Table 3. Sensing Performances of the ID-eSRR and eSRR MMs**

Structure	Analyte Thickness (nm)	$S$ (GHz/RIU)	FOM (RIU <sup>-1</sup> )	TN-FOM ( $\mu\text{m}^{-1}$ RIU <sup>-1</sup> )
ID-eSRR	100	22.6	3.29	32.87
	500	63.0	9.16	18.33
	1000	70.1	10.20	10.20
eSRR ( $G = 0.6 \mu\text{m}$ )	100	5.9	0.22	2.18
	500	20.5	0.76	1.52
	1000	27.7	1.02	1.02
eSRR ( $G = 12 \mu\text{m}$ )	100	1.6	0.03	0.31
	500	6.3	0.12	0.25
	1000	10.5	0.21	0.21

stored in the resonator. For example, this factor is only 11.6% for the ID-eSRR structure and 1.76% for the eSRR structure with  $G = 0.6 \mu\text{m}$ . Increasing the high-electric-field area does not proportionally increase the total energy (detailed information regarding this factor is provided in Appendix C). From those numbers and according to Eq. (2), the sensitivity and the TN-FOM of the ID-eSRR structure are estimated to increase by about 3.5 and 15 times, respectively, compared to those of the small-gap eSRR.

### B. Simulated Performances of Thin Film Sensing

The resonance frequency experiences a redshift when a homogeneous layer of dielectric analyte is deposited onto the MM. The extent of frequency shift depends on the thickness and refractive index of the analyte. We perform CST simulations for an analyte for which we assume its complex-valued relative permittivity to be  $3.75 + j \cdot 0.0004$  (equal to that of the fused silica substrate). We assume in the simulations that the analyte is an interrupted layer, as shown in the inset of Fig. 3(b). Figure 3(b) compares the resonance frequency shift of the ID-eSRR and eSRR MMs as a function of the thickness of the analyte layer (20 to 1000 nm). The resonance frequency shift exhibits a nonlinear relationship with the analyte thickness due to the exponential decay of the evanescent electric field from the metal surface to the upper air region [31]. Therefore, as the analyte thickness increases, the frequency shift initially rises rapidly, and then increases more gradually before eventually saturating. When the analyte thickness is 100 nm, the frequency shift for the ID-eSRR structure is 21.1 GHz, which is 14.1 times that of the large-gap eSRR structure and 3.8 times that of the eSRR structure with the small gap. With an analyte thickness of 1000 nm, the frequency shift for the ID-eSRR

structure increases to 66.1 GHz, which is 2.6 times (respectively, 6.7 times) the value for the large-gap (small-gap) eSRR structure. The ID-eSRR MM sensor promises hence to be much more sensitive than the eSRR MM sensors, especially so if the analyte layer is thin.

Table 3 compares the calculated values of the sensitivity  $S$  (in GHz/RIU), the figure of merit (FOM, in units of RIU<sup>-1</sup>), and the thickness normalized FOM (TN-FOM, in units of  $\mu\text{m}^{-1}$  RIU<sup>-1</sup>) of the three sensors. The ID-eSRR MMs exhibit advantages in terms of high values of the  $Q$ -factor, sensitivity, and FOM. When the analyte thickness is 100 nm, the sensitivity of the ID-eSRR structure is 3.8 times, and the FOM (TN-FOM) value is 15.1 times that of the small-gap eSRR MM. The numbers from these independent simulations are consistent with the estimations from Eq. (2), as mentioned in the previous section, confirming the validity of perturbation theory. Putting this performance into perspective with the literature on MM sensors, we note that the ID-eSRR MM has a higher sensitivity for a layer thickness of 100 nm than what the device of Ref. [14] reaches for an analyte thickness of  $2.17 \mu\text{m}$  (8.1 GHz/RIU). It should be noted that the frequency shift and sensitivity of the ID-eSRR structure can be further enhanced by decreasing the width of the minigaps ( $g$ ). Additional information regarding this improvement is provided in Appendix D.

### C. Proof-of-Principle Experiment

The scanning-electron-microscope (SEM) image of a single ID-eSRR resonator is shown in Fig. 5(a). In Figs. 5(b) and 5(c), we present the simulated and measured transmittance spectra, respectively, for both types of MM sensors. The agreement among the resonance frequencies, the amplitudes, and the shapes of the simulated and measured spectra is quite

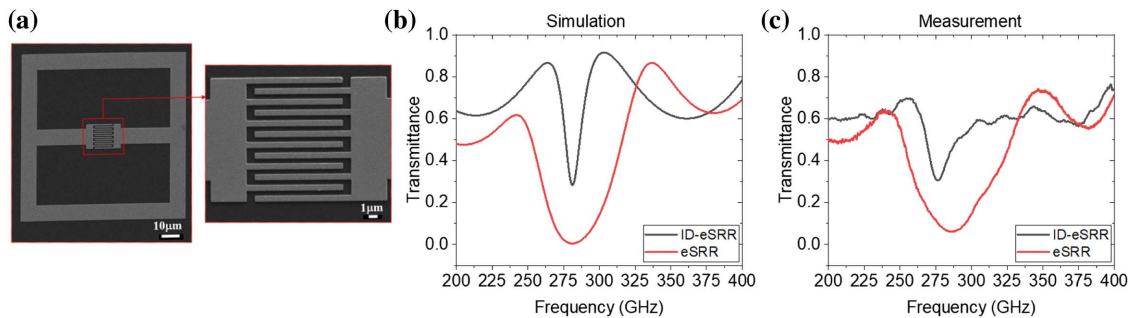


**Fig. 5.** (a) SEM image of an ID-eSRR structure fabricated by electron beam lithography. (b) Simulated transmittance spectra of the ID-eSRR MM ( $G = 12 \mu\text{m}$ ;  $w = g = 0.6 \mu\text{m}$ ) and the eSRR MM ( $G = 12 \mu\text{m}$ ) without analyte. (c) Measured transmittance spectra of the ID-eSRR and eSRR MMs without analyte.

satisfactory. The remaining discrepancies may stem from the different illumination conditions in the simulations and measurements: the simulations assume a plane wave with a well-defined wave vector, while the measurements are performed with a focused THz beam with an angular spread of wave vectors, for which the MM's response may vary (further details are provided in Appendix E). Additional deviations may arise from different values of the substrate permittivity and the metal conductivity in the experiment and simulations as well as fabrication tolerances, particularly with regard to the metal fingers.

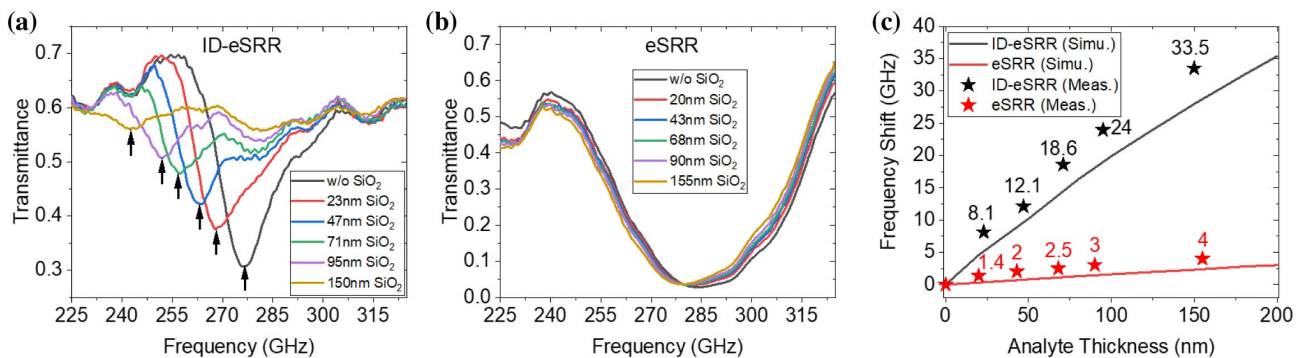
Figures 6(a) and 6(b) present the measured transmittance spectra for the empty and analyte-loaded ID-eSRR and eSRR structures. Data for five distinct values of the SiO<sub>2</sub> layer thickness are shown. These are for the ID-eSRR sensor 23, 47, 71, 95, and 150 nm, and for the eSRR sensor 20, 43, 68, 90, and 155 nm. For each spectrum, we determine the respective resonance frequency. In the case of the ID-eSRR sensor, this is simply the frequency position of the transmission minimum [marked by an upward-pointing black arrow in Fig. 6(a)]. For the eSRR sensor, the minimum is difficult to identify directly. We determine it by fitting the resonance curve with a Lorentzian function around the broad transmission valley. It is obvious that the presence of the analyte leads to a much stronger shift of the resonance frequency in the case of the ID-eSRR MM as compared with the eSRR MM. It should be noted that the resonance depth of the ID-eSRR sensor decreases with the increase of analyte thickness. This modulation is mainly caused by the Fabry–Perot resonance within the thick substrate. Further details are provided in Appendix F.

Figure 6(c) displays the resultant frequency shifts for the two structures. For comparison, we also include the simulated frequency shifts. Theory and experiment confirm the superior sensitivity of the ID-eSRR structure. At a thickness of around 20 nm, the ID-eSRR structure exhibits a measured frequency shift of 8.1 GHz, compared with a value of 1.4 GHz for the eSRR structure, a nearly six times better performance. For a thickness of about 150 nm, this ratio is even larger, reaching a value of 8.4. There, the *Q*-factor, sensitivity, and FOM value of the ID-eSRR structure are higher by factors of 6.6, 8.4, and 55.3, respectively. For both structures, a weak trend toward saturation is observed.

#### 4. DISCUSSION

One notices in Fig. 6(c) that the measured frequency shift is always larger than the calculated one. We attribute this systematic difference to the treatment of the analyte layer in the simulations as an interrupted film [Fig. 3(b)]. Because the film thickness is inferior to the MM thickness (200 nm), there always exists additional analyte on vertical edges (the *yo**z* plane) of fingers in the sputtering process, which cannot be properly considered in the simulation. As the electric field is strongly concentrated in that gap, the simulations underestimate the strength of the interaction between the field and the analyte material.

We now come to a comparison of the measured performance parameters of the ID-eSRR MM sensor with the literature. In Table 4, we list analyte thicknesses, resonance



**Fig. 6.** (a) Measured transmittance spectra of the ID-eSRR structure loaded with a SiO<sub>2</sub> layer of varying thickness (from 23 to 150 nm). (b) Likewise, but for the eSRR structure (SiO<sub>2</sub> layer thickness varying from 20 to 155 nm). (c) Simulated and measured resonance frequency shift in dependence of the SiO<sub>2</sub> layer thickness.

**Table 4.** Performance Comparison with Other THz Metamaterial Sensors Described in the Literature<sup>a</sup>

Analyte Thickness	$f_0$ (GHz)	$Q$	$S$ (GHz/RIU)	FOM (RIU <sup>-1</sup> )	TN-FOM (μm <sup>-1</sup> RIU <sup>-1</sup> )	Unit Cell Structure	Reference
2.17 μm	407	4	8.1	0.08	0.04	SRR	[14]
1 μm	515	28 <sup>b</sup>	16.7	0.91 <sup>b</sup>	0.91 <sup>b</sup>	aDSRR	[10]
345 nm	136.5	11.8	7.5	0.65	1.88	Labyrinth	[47]
250 nm	422.6	9.6 <sup>b</sup>	6.0	0.14 <sup>b</sup>	0.54 <sup>b</sup>	Toroidal aDSRR	[48]
240 nm	600	10 <sup>b</sup>	18.0	0.30 <sup>b</sup>	1.25 <sup>b</sup>	I-shaped structure	[17]
40 nm	990	20	10.8	0.22	5.45	aDSRR	[39]
47 nm	276	17.7	12.1	0.78	16.51	ID-eSRR	This work
150 nm	276	17.7	33.5	2.15	14.32	ID-eSRR	This work

<sup>a</sup>Data derived from experiments.

<sup>b</sup>Simulation values are used because the experimental values are not available.

frequencies,  $Q$ -factors,  $S$ , and FOM (TN-FOM) values as well as the unit cell structures of various MM sensors. Where experimental data are not available, we list simulation results taken from the publications. When making comparisons, one should bear in mind that the respective literature studies have been performed not only at different resonance frequencies but also for different types of analytes and values of the analyte thickness. As already demonstrated by the simulation results for our sensors in Table 3,  $S$  and FOM (which correct for the different refractive-index values of the various analytes) increase with analyte thickness, which is a feature that is also true for the sensors studied in the literature.

However, Table 4 still allows us to make statements on the relative performance of the ID-eSRR MM. At an analyte thickness of 150 nm, the FOM value of the ID-eSRR structure outperforms that of all other reported sensors, most of which were subjected to the tests with thicker layers. Only for one MM, the literature reports measurements at small thickness; this is the aDSRR (quasi-BIC) sensor of Ref. [39], a state-of-the-art device whose operation principle is based on a Fano resonance. To keep the field concentrated above the substrate, it was built on a membrane with a low dielectric constant; the resonance frequency was chosen high (990 GHz) for a high field extension into the air. Even so, it reaches, at an analyte thickness of 40 nm, a value of  $S$  that is quite similar to that obtained with our ID-eSRR MM at a thickness of 47 nm; however, the FOM and TN-FOM achieved with the ID-eSRR sensor are considerably higher.

Finally, we compare with the performance parameters of the I-shaped sensor of Ref. [17], which was also operated at a higher resonance frequency (approximately 600 GHz) than our ID-eSRR device. For a  $\text{SiO}_2$  layer thickness of 150 nm, the latter reaches better values of  $S$  and FOM than what were obtained with the I-shaped sensor at a  $\text{SiO}_2$  layer thickness of 240 nm. From Figs. 6(a) and 6(c) and Ref. [17], we find that the ID-eSRR MM sensor reaches about the same absolute frequency shift (18.6 GHz) as the I-shaped sensor but already for a  $\text{SiO}_2$  layer thickness of 71 nm instead of 240 nm and this at a much lower resonance frequency.

These results corroborate the exceptional sensitivity of the proposed ID-eSRR sensor in detecting analytes and that it is especially well-suited for low analyte thickness.

## 5. CONCLUSION

In conclusion, we have proposed a general optimization method for designing high-performance planar metamaterial sensors operating at terahertz frequencies. This method relies on simplified dielectric perturbation theory. By utilizing resonators with high  $Q$ -factors, reduced mode volumes, and enhanced overlap volume between the high-electric-field region and the analyte material, sensor sensitivity can be significantly improved. This approach serves as a versatile method for the sensitive detection of thin dielectric films and minute traces of molecules.

As a demonstration and application of dielectric perturbation theory, we designed a sensitive metamaterial-based terahertz sensor for thin-film analytes. The metamaterial's unit cell comprises an electric split-ring resonator with a gap in

the metal stripes implemented as an interdigitated finger structure. The device is tailored for a resonance frequency of 0.3 THz. In comparison with its parent metamaterial featuring a slot-like gap (denoted as length  $G$  in the main text) instead of the meander-like gap between interdigitated fingers, the novel structure exhibits a significantly higher  $Q$ -factor and strong electric-field enhancement over a sizable area. Consequently, this leads to a significantly enhanced sensitivity, FOM, and thickness-normalized FOM. In a proof-of-principle experiment involving a  $\text{SiO}_2$  analyte layer, we observed a more than fifty-fold increase in FOM (TN-FOM).

This innovative sensor holds promise for label-free and amplification-free detection of trace amounts of analytes, particularly biomolecules such as DNA and proteins. Importantly, the sensors can be implemented across a wide range of frequencies due to the frequency-scalable nature of the design.

## 6. METHODS

### A. Electromagnetic Simulations

We use the CST Studio Suite (Dassault Systèmes) with a frequency-domain solver to compute the transmittance spectra of the three MM structures across the frequency range of 200 to 400 GHz. In simulations, the MM structure is modeled with periodic boundary conditions along the  $x$  and  $y$  directions and a perfectly matched layer along the  $z$  direction. The thickness of the gold metallization is assumed to be 200 nm, with a conductivity of gold of  $4.56 \times 10^7$  S/m. The substrate material is fused silica with a thickness of 150  $\mu\text{m}$ , characterized by a relative permittivity of 3.75 and a loss tangent of 0.0004. The incident THz radiation is polarized along the direction of the interdigitated fingers ( $x$  direction in Fig. 2).

### B. Sample Fabrication

To validate the simulation results, we fabricated two MMs via electron beam lithography (EBL). One of them features an ID-eSRR design with parameters  $G = 12 \mu\text{m}$  and  $w = g = 0.6 \mu\text{m}$ . The other structure serves as a reference; it has an eSRR configuration and a gap without fingers with  $G = 12 \mu\text{m}$ . The ID-eSRR MM consists of  $18 \times 18$  unit cells, while the eSRR MM has  $12 \times 12$  unit cells, and the two MMs have a size of  $3.076 \text{ mm} \times 3.076 \text{ mm}$ . The substrate is 500  $\mu\text{m}$  thick. The fabrication process started with the deposition of a thick layer of polymethyl methacrylate (PMMA) 950A11 (1.8  $\mu\text{m}$ ) on a fused silica substrate with a size of  $40 \text{ mm} \times 40 \text{ mm}$ . Due to the transparent nature of the fused silica, an additional photoconductive polymer layer (40 nm) was deposited over the PMMA layer (AR-PC 5092.02). Two EBL exposure steps were performed to design the MMs. The first exposure was used to create the markers used to detect the sample height in the EBL machine. The second exposure was performed to create the MMs with different features. After each exposure, metallization lift-off processes were performed. The 10/200 nm thick Cr/Au films were deposited by e-beam evaporation after the second EBL exposure.

### C. Terahertz Characterization

Transmission THz measurements are performed with a continuous-wave THz spectroscopy system operating in the

frequency domain. This system is based on a TeraScan 1550 system from TOPTICA Photonics AG, which offers high bandwidth, high dynamic range, and spectral resolution of 1 MHz [49]. To adapt it for the characterization of the MM sensors, four off-axis parabolic mirrors (focal length of 4 in. and diameter of 2 in.) are incorporated to create a quasi-optical transmission path with an intermediate focal plane, where the MM sensor is positioned. A vacuum holder for the specimens is mounted on motorized linear stages (MICOS LS-65). It is designed to enable reproducible, precise mounting of the MMs. During all measurements, spectral scans are performed with a scan speed of 240 GHz/min and a lock-in integration time of 10 ms. All scans are repeated five times, and the mean value is taken for the evaluation and plotting of the transmission spectra.

#### D. Deposition of a Nanoscale Thin Film Analyte

In order to assess the sensitivity of the sensors, we deposit layers of  $\text{SiO}_2$  with varying thickness onto the sensor surface using a self-built RF magnetron sputtering chamber with a  $\text{SiO}_2$  target, offering a sputtering rate of around 0.25 nm/s. We begin with a thin layer, then measure the transmittance, and then deposit more  $\text{SiO}_2$  onto the specimen for the next measurement cycle. This process is repeated several times. During each sequence, the actual thickness of the  $\text{SiO}_2$  layer is determined with a surface profilometer (Bruker NanoDektak). Before each sputtering process as well as before each THz measurement, the MM sensor is cleaned with acetone (3 min) and isopropanol (3 min) and then dried in nitrogen gas flow to ensure that the surface of the sensor is free from contamination.

#### APPENDIX A: RADIATION PATTERN

To specifically investigate the impact of finger structures on radiation loss, a single resonator of ID-eSRR and eSRR with a perfect conductor suspended in air is excited, and the far-field radiation pattern is captured on a sphere placed 1 m away from the resonator [50]. Figure 7 illustrates the 3D distribution of the three single resonators at their respective resonance frequencies. It is evident from the figure that the radiation pattern resembles that of a pure electric dipole oriented in the  $x$  direction. Consequently, radiation along the  $x$  direction is minimal, while radiation along the  $y$  and  $z$  directions has nearly identical values. The interdigitated eSRR structure exhibits the lowest radiation among all structures. Additionally, the eSRR structure with a narrow gap width demonstrates slightly smaller radiation loss. In order to quantitatively compare the radiation power, Fig. 8 illustrates the radiation power density in different projection planes, namely  $x$ - $y$ ,  $y$ - $z$ , and  $x$ - $z$ . The interdigitated eSRR significantly reduces radiation along the  $y$  and  $z$  axes, while the eSRR with a smaller gap always maintains radiation within the pattern of the eSRR with a larger gap. This implies that radiation can be effectively reduced with the inclusion of interdigitated fingers, aligning with the  $Q$ -factor influenced by radiation loss (Table 2 in the main text). For instance, the power flow (in  $\text{W}/\text{m}^2$ ) along the  $y$  direction is  $-22.96$  dB (ID-eSRR),  $-12.47$  dB (eSRR with  $G = 0.6 \mu\text{m}$ ), and  $-11.22$  dB (eSRR with  $G = 12 \mu\text{m}$ ). Further, the reduction of radiation loss can be understood intuitively by the fact that neighboring fingers always have opposite signs of net charge at any given instant, resulting in opposite electric field directions in neighboring minigaps, thereby greatly reducing the strength

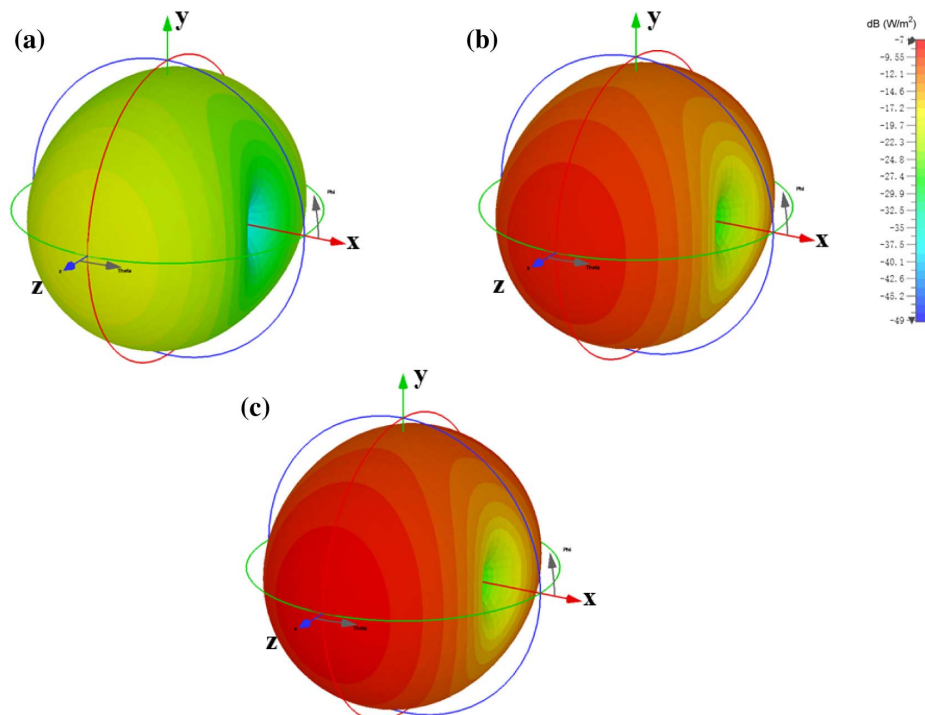


**Fig. 7.** Radiation power flow on a sphere with a radius of 1 m for a single resonator in air: (a) ID-eSRR; (b) eSRR ( $G = 0.6 \mu\text{m}$ ); and (c) eSRR ( $G = 12 \mu\text{m}$ ).

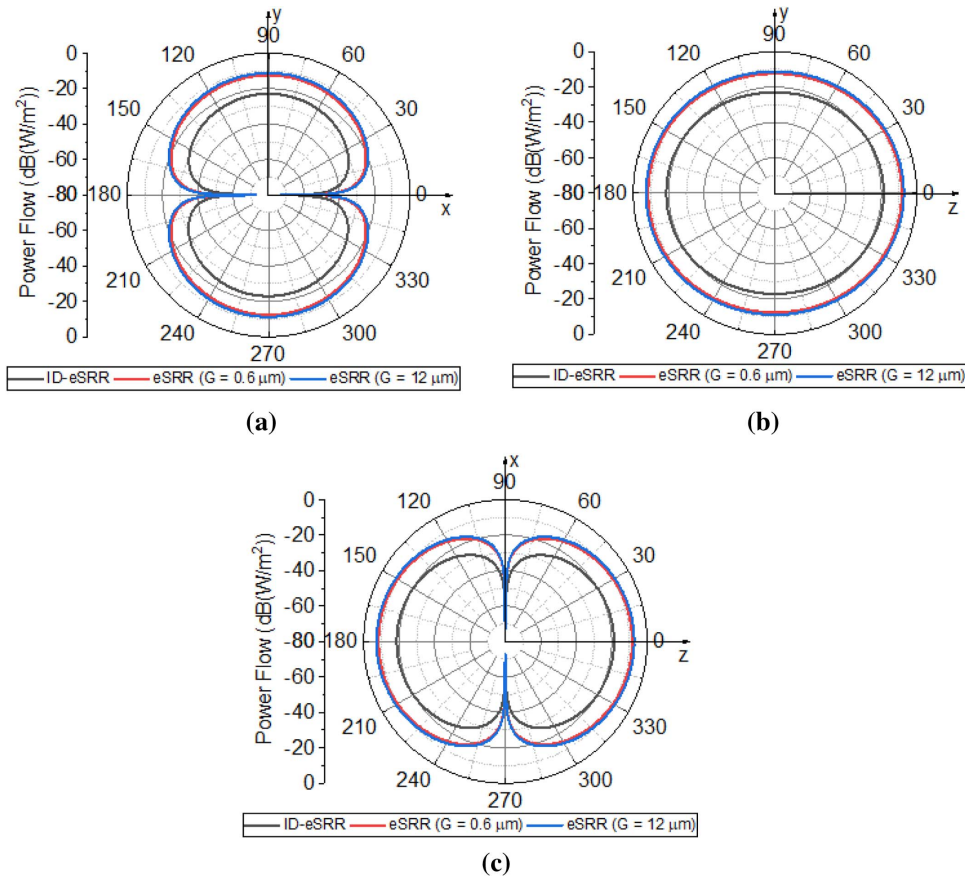


**Fig. 8.** 2D projection of the radiation power flow of a single resonator in air: (a)  $x$ - $y$  plane; (b)  $y$ - $z$  plane; and (c)  $x$ - $z$  plane.

of the net electric dipole. In the case of the ID-eSRR structure, the primary origin of loss is only the conduction loss; therefore, the  $Q$ -factor of the ID-eSRR structure is higher than that of eSRR structures where radiation and conduction losses dominate in total losses.

**APPENDIX B: ELECTRIC FIELD DISTRIBUTION ALONG Z AXIS**

Figure 9 shows the electric field enhancement factor (electric field in MMs normalized by the incident electric field) for the three structures along the  $z$  axis around the metal corners in the gap region where the electric field is maximal. The ID-eSRR structure and eSRR structure with  $G = 0.6 \mu\text{m}$  exhibit comparable electric field extension profiles along the propagation direction of the THz wave ( $z$  axis) and a maximal electric field enhancement factor (1200), which is at least five times higher than that of the eSRR structure with  $G = 12 \mu\text{m}$ . If we define a critical distance as the  $z$  position where the electric field intensity decays to half of the electric field intensity at the metal surface, this critical distance is lower than 200 nm for the ID-eSRR structure and eSRR structure with  $G = 0.6 \mu\text{m}$ , while it is greater than  $5 \mu\text{m}$  for the eSRR structure with  $G = 12 \mu\text{m}$ . This means that structures with narrow gaps (ID-eSRR and eSRR structure with  $G = 0.6 \mu\text{m}$ ) are well-suited for the sensitive detection of analytes with thicknesses ranging from several tens to hundreds of nanometers.

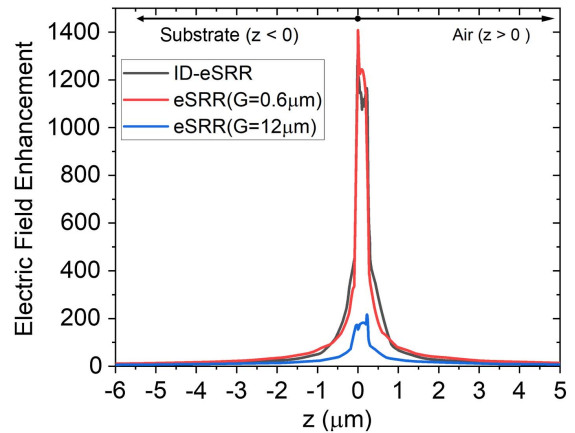


**Fig. 9.** Electric field enhancement factor ( $E_{\text{max}}/E_{\text{in}}$ ) along the  $z$  axis around the metal corner where the electric field is maximal at resonance frequencies for the three structures:  $z < 0$  represents the substrate side; and  $z > 0$  represents the air side.

**APPENDIX C: GAP ELECTRIC ENERGY FACTOR**

In order to quantitatively calculate the influence of high electric field region on the frequency shift, we introduce a new specification parameter “gap electric energy factor,” defined by the

ratio between the electric energy within the gap and the total energy within the resonator,

$$F_e = \frac{W_{\text{gap}}}{W_0} = \frac{\int_{V_{\text{gap}}} \epsilon_0 |\vec{E}_0|^2 dV}{W_0}, \quad (\text{C1})$$

where  $\epsilon_0$  is the vacuum permittivity, and  $W_0$  is the total energy stored in the cavity per unit cell. The lateral size of the integration volume ( $V_{\text{gap}}$ ) in the numerator is  $b \times G$ . By performing volume integral up to distance of 30  $\mu\text{m}$  above and below the plane of MMs ( $z = 0$ ), this factor ( $F_e$ ) is calculated to be 11.6% (ID-eSRR), 1.76% (eSRR with  $G = 0.6 \mu\text{m}$ ), and 0.74% (eSRR with  $G = 12 \mu\text{m}$ ). The extremely high value of  $F_e$  for the proposed interdigitated MM structure indicates that it will be much more sensitive to the analyte perturbation in the gap region for sensing applications. This also means that the total energy and the corresponding mode volume will not increase at the same speed as the gap electric energy.

#### APPENDIX D: INFLUENCES OF MINIGAP WIDTH

The performance of the ID-eSRR MM sensor is closely related to its structural parameters, especially the minigap width ( $g$ ). Keeping other structural parameters constant, Fig. 10 shows the relationship between transmittance and frequency shift with the gap width  $g = 0.2\text{--}1.2 \mu\text{m}$ . As the minigap width increases, the equivalent capacitance decreases, and the resonance frequency moves to a higher frequency, while the resonance depth increases. At the same time, the amplitude of the electric field in minigaps decreases, and the frequency shift reduces from 14.6 GHz (0.2  $\mu\text{m}$ ) to 8.8 GHz (1.2  $\mu\text{m}$ ) accordingly. Therefore, reducing the minigap width is beneficial for increasing the electric field amplitude during MM resonance, thereby greatly enhancing sensing sensitivity, especially for ultrathin analytes. However, it also increases the complexity of fabrication processes and the associated costs, often requiring the use of electron beam lithography.

#### APPENDIX E: INFLUENCES OF THE INCIDENT ANGLE OF THz RADIATION ON TRANSMISSION SPECTRA

Figure 11 shows the simulated transmittance curves at different values of the incident angle of THz radiation. With the increase

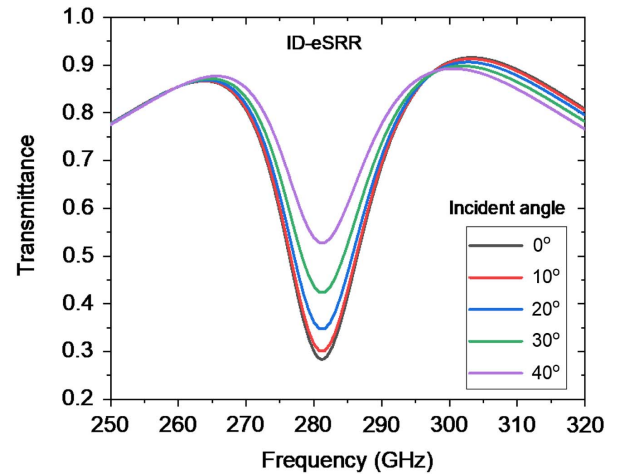


**Fig. 11.** Transmittance spectra for the ID-eSRR MMs sensor at different incident angle of THz radiation.

in the incident angle, the resonance depth and the  $Q$ -factor decrease. In the measurement, the incident angle of the focused THz beam varies between 0 and 6.5 deg, estimated from the size of the THz beam and the focal length of the off-axis parabolic mirror. This is one reason to explain the small deviation between simulation and experimental results.

#### APPENDIX F: INFLUENCES OF THE ANALYTE THICKNESS ON TRANSMISSION SPECTRA

In addition to the cause of frequency shift, the amount of analyte will also influence the resonance depth. Figure 12 shows the simulated transmittance spectra for the ID-eSRR MMs sensor with the variation of analyte thickness up to 20  $\mu\text{m}$ . When the LC resonance in ID-eSRR MMs (zero analyte thickness) coincides with the transmission peak at around 285 GHz (Fabry–Perot resonance in the 500  $\mu\text{m}$  thick substrate), the resonance depth is maximal. At this frequency, the electric field amplitude has the maximal value at the interface of substrate/top air, which helps to strengthen the LC resonance depth. With the increase of analyte thickness to 0.6  $\mu\text{m}$ , the LC resonance depth of the ID-eSRR MMs reaches the minimal value, and the resonance shifts to a lower frequency around

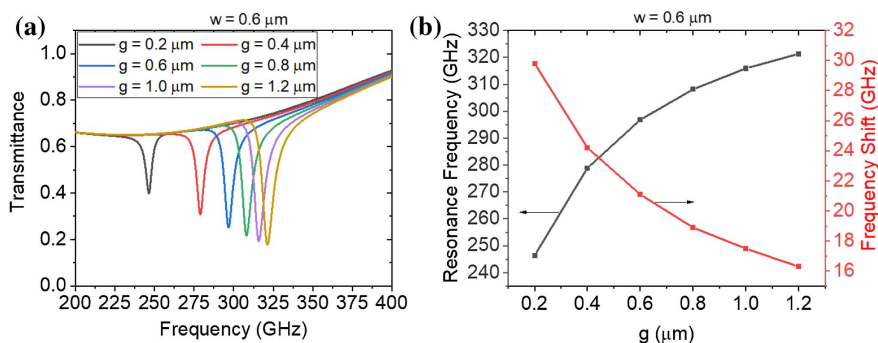


**Fig. 10.** Influences of minigap width ( $g$ ) on the transmittance spectra and resonance frequencies. (a) Transmittance spectra with the variation of  $g$  from 0.2 to 1.2  $\mu\text{m}$ , while the finger width kept constant ( $w = 0.6 \mu\text{m}$ ). (b) Resonance frequency and frequency shift when 100 nm  $\text{SiO}_2$  is deposited on the unit cell structure.

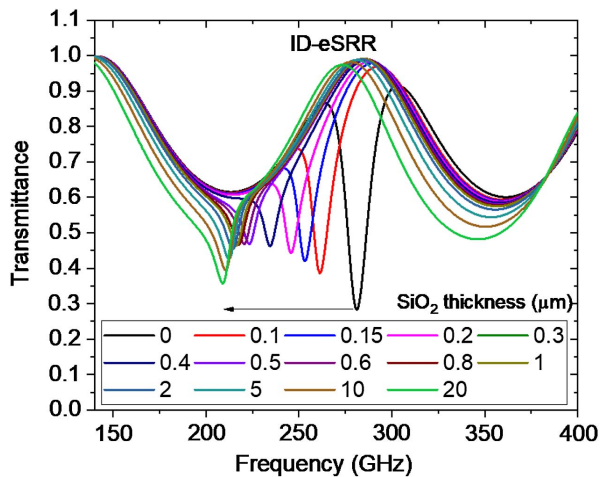


**Fig. 12.** Transmittance spectra for the ID-eSRR MMs sensor with the variation of analyte ( $\text{SiO}_2$ ) thickness from 0 (no analyte) to 20  $\mu\text{m}$ .

220 GHz, corresponding to the transmission valley at which frequency the electric field amplitude has the minimal value at the interface of substrate/top air. With a further increase in analyte thickness, the resonance depth starts to increase. This modulation effect of analyte thickness on the transmission depth can be alleviated by using a thin substrate with a low refractive index.

**Funding.** Deutsche Forschungsgemeinschaft (HA 3022/15-1, RO 770/46-1, RO 770/50-1).

**Acknowledgment.** L. Cao acknowledges support from the HUST Overseas Training Program for Outstanding Young Teachers. The computation was completed in the HPC Platform of Huazhong University of Science and Technology.

**Disclosures.** The authors declare no conflicts of interest.

**Data Availability.** Data underlying the results presented in this paper are not publicly available at this time but may be obtained from the first author upon reasonable request.

## REFERENCES

- A. Lahav, M. Auslender, and I. Abdulhalim, "Sensitivity enhancement of guided-wave surface-plasmon resonance sensors," *Opt. Lett.* **33**, 2539–2541 (2008).
- E. S. Yu, S. H. Lee, G. Lee, *et al.*, "Nanoscale terahertz monitoring on multiphase dynamic assembly of nanoparticles under aqueous environment," *Adv. Sci.* **8**, 2004826 (2021).
- Y.-M. Bahk, K.-H. Kim, K. J. Ahn, *et al.*, "Recent developments in terahertz nanosensors," *Adv. Photon. Res.* **5**, 2300211 (2023).
- F. Vollmer and L. Yang, "Label-free detection with high-Q microcavities: a review of biosensing mechanisms for integrated devices," *Nanophotonics* **1**, 267–291 (2012).
- W. Yu, W. C. Jiang, Q. Lin, *et al.*, "Cavity optomechanical spring sensing of single molecules," *Nat. Commun.* **7**, 12311 (2016).
- N. P. Mauranyapin, L. S. Madsen, M. A. Taylor, *et al.*, "Evanescent single-molecule biosensing with quantum-limited precision," *Nat. Photonics* **11**, 477–481 (2017).
- W. Withayachumnankul and D. Abbott, "Metamaterials in the terahertz regime," *IEEE Photon. J.* **1**, 99–118 (2009).
- C. Debus and P. H. Bolivar, "Frequency selective surfaces for high sensitivity terahertz sensing," *Appl. Phys. Lett.* **91**, 184102 (2007).
- I. A. I. Al-Naib, C. Jansen, and M. Koch, "Thin-film sensing with planar asymmetric metamaterial resonators," *Appl. Phys. Lett.* **93**, 083507 (2008).
- R. Singh, W. Cao, I. Al-Naib, *et al.*, "Ultrasensitive terahertz sensing with high-Q Fano resonances in metasurfaces," *Appl. Phys. Lett.* **105**, 171101 (2014).
- C. Weisenstein, D. Schaar, A. K. Wigger, *et al.*, "Ultrasensitive THz biosensor for PCR-free CDNA detection based on frequency selective surfaces," *Biomed. Opt. Express* **11**, 448–460 (2020).
- S. J. Park, S. H. Cha, G. A. Shin, *et al.*, "Sensing viruses using terahertz nano-gap metamaterials," *Biomed. Opt. Express* **8**, 3551–3558 (2017).
- F. Meng, F. Han, U. Kentsch, *et al.*, "Coherent coupling of metamaterial resonators with dipole transitions of boron acceptors in Si," *Opt. Lett.* **47**, 4969–4972 (2022).
- W. Withayachumnankul, H. Lin, K. Serita, *et al.*, "Sub-diffraction thin-film sensing with planar terahertz metamaterials," *Opt. Express* **20**, 3345–3352 (2012).
- M. Islam, S. J. M. Rao, G. Kumar, *et al.*, "Role of resonance modes on terahertz metamaterials based thin film sensors," *Sci. Rep.* **7**, 7355 (2017).
- S. W. Jun and Y. H. Ahn, "Terahertz thermal curve analysis for label-free identification of pathogens," *Nat. Commun.* **13**, 3470 (2022).
- M. Gupta and R. Singh, "Terahertz sensing with optimized  $Q/V_{\text{eff}}$  metasurface cavities," *Adv. Opt. Mater.* **8**, 1902025 (2020).
- T. Driscoll, G. O. Andreev, D. N. Basov, *et al.*, "Tuned permeability in terahertz split-ring resonators for devices and sensors," *Appl. Phys. Lett.* **91**, 062511 (2007).
- I. Al-Naib, "Biomedical sensing with conductively coupled terahertz metamaterial resonators," *IEEE J. Quantum Electron.* **23**, 4700405 (2017).
- B. Jin, W. Tan, C. Zhang, *et al.*, "High-performance terahertz sensing at exceptional points in a bilayer structure," *Adv. Theory Simul.* **1**, 1800070 (2018).
- J. Ma, S. Wang, Y. Yang, *et al.*, "Simulation of terahertz-band metamaterial sensor for thin film analyte detection," *AIP Adv.* **10**, 085227 (2020).
- L. Sun, L. Xu, J. Y. Wang, *et al.*, "A pixelated frequency-agile metasurface for broadband terahertz molecular fingerprint sensing," *Nanoscale* **14**, 9681–9685 (2022).
- F. Meng, L. Cao, A. Karalis, *et al.*, "Strong coupling of plasmonic bright and dark modes with two eigenmodes of a photonic crystal cavity," *Opt. Express* **31**, 39624–39637 (2023).
- W. He, Y. Hu, Z. Ren, *et al.*, "Transient loss-induced non-Hermitian degeneracies for ultrafast terahertz metadevices," *Adv. Sci.* **10**, 2304972 (2023).
- M. Tang, L. Xia, D. Wei, *et al.*, "Rapid and label-free metamaterial-based biosensor for fatty acid detection with terahertz time-domain spectroscopy," *Spectrochim. Acta A* **228**, 117736 (2020).
- M. Gezimati and G. Singh, "Terahertz cancer imaging and sensing: open research challenges and opportunities," *Opt. Quantum Electron.* **55**, 727 (2023).
- C. Weisenstein, A. K. Wigger, M. Richter, *et al.*, "THz detection of biomolecules in aqueous environments: status and perspectives for analysis under physiological conditions and clinical use," *J. Infrared Millim. Terahertz Waves* **42**, 607–646 (2021).
- M. Richter, Y. Loth, C. Weisenstein, *et al.*, "Ultrasensitive marker-free biomolecular thz-detection for tumor-related analytics," *Frequenz* **76**, 627–637 (2022).
- M. Askari, H. Pakarzadeh, and F. Shokrgozar, "High Q-factor terahertz metamaterial for superior refractive index sensing," *J. Opt. Soc. Am. B* **38**, 3929–3936 (2021).
- D. Pozar, *Microwave Engineering*, 4th ed. (Wiley, 2011).
- L. Cao, S. Jia, M. D. Thomson, *et al.*, "Can a terahertz metamaterial sensor be improved by ultra-strong coupling with a high-Q photonic resonator?" *Opt. Express* **30**, 13659–13672 (2022).

32. M. A. Seo, H. R. Park, S. M. Koo, *et al.*, "Terahertz field enhancement by a metallic nano slit operating beyond the skin-depth limit," *Nat. Photonics* **3**, 152–156 (2009).
33. Y.-M. Bahk, S. Han, J. Rhie, *et al.*, "Ultimate terahertz field enhancement of single nanoslits," *Phys. Rev. B* **95**, 075424 (2017).
34. S. Adak and L. N. Tripathi, "Nanoantenna enhanced terahertz interaction of biomolecules," *Analyst* **144**, 6172–6192 (2019).
35. C. Gerry and P. Knight, *Introductory Quantum Optics* (Cambridge University, 2004).
36. X. Yan, M. S. Yang, Z. Zhang, *et al.*, "The terahertz electromagnetically induced transparency-like metamaterials for sensitive biosensors in the detection of cancer cells," *Biosens. Bioelectron.* **126**, 485–492 (2019).
37. M. Abdolrazzagli, M. Daneshmand, and A. K. Iyer, "Strongly enhanced sensitivity in planar microwave sensors based on metamaterial coupling," *IEEE Trans. Microw. Theory Tech.* **66**, 1843–1855 (2018).
38. Y. Cao, C. Ruan, K. Chen, *et al.*, "Research on a high-sensitivity asymmetric metamaterial structure and its application as microwave sensor," *Sci. Rep.* **12**, 1255 (2022).
39. Y. K. Srivastava, R. T. Ako, M. Gupta, *et al.*, "Terahertz sensing of 7 nm dielectric film with bound states in the continuum metasurfaces," *Appl. Phys. Lett.* **115**, 151105 (2019).
40. M. F. Limonov, M. V. Rybin, A. N. Poddubny, *et al.*, "Fano resonances in photonics," *Nat. Photonics* **11**, 543–554 (2017).
41. Y. Hu, M. Tong, S. Hu, *et al.*, "Reassessing Fano resonance for broadband, high-efficiency, and ultrafast terahertz wave switching," *Adv. Sci.* **10**, 2204494 (2023).
42. D. R. Abujetas, N. van Hoof, S. ter Huurne, *et al.*, "Spectral and temporal evidence of robust photonic bound states in the continuum on terahertz metasurfaces," *Optica* **6**, 996–1001 (2019).
43. J. Ding, L. Huang, Y. Luo, *et al.*, "Multi-band polarization-independent quasi-bound states in the continuum based on tetramer-based metasurfaces and their potential application in terahertz microfluidic bio-sensing," *Adv. Opt. Mater.* **11**, 2300685 (2023).
44. F. Yang, J. Li, L. Wu, *et al.*, "Bending sensing based on quasi bound states in the continuum in flexible terahertz metasurface," *Adv. Opt. Mater.* **11**, 2300909 (2023).
45. D. Schurig, J. J. Mock, and D. R. Smith, "Electric-field-coupled resonators for negative permittivity metamaterials," *Appl. Phys. Lett.* **88**, 041109 (2006).
46. W. Withayachumnankul, C. Fumeaux, and D. Abbott, "Compact electric-LC resonators for metamaterials," *Opt. Express* **18**, 25912–25921 (2010).
47. I. Jáuregui-López, P. Rodríguez-Ulibarri, A. Urrutia, *et al.*, "Labyrinth metasurface absorber for ultra-high-sensitivity terahertz thin film sensing," *Phys. Status Solidi* **12**, 1800375 (2018).
48. M. Gupta, Y. K. Srivastava, M. Manjappa, *et al.*, "Sensing with toroidal metamaterial," *Appl. Phys. Lett.* **110**, 121108 (2017).
49. A. J. Deninger, A. Roggenbuck, S. Schindler, *et al.*, "2.75 THz tuning with a triple-DFB laser system at 1550 nm and InGaAs photomixers," *J. Infrared Millim. Terahertz Waves* **36**, 269–277 (2015).
50. T. Q. Li, H. Liu, T. Li, *et al.*, "Suppression of radiation loss by hybridization effect in two coupled split-ring resonators," *Phys. Rev. B* **80**, 115113 (2009).